RSC Advances

PAPER

View Article Online
View Journal | View Issue

Cite this: *RSC Adv.*, 2024, **14**, 24928

Crystal structure, spectroscopy, DFT, and thermal studies of 3-cyano-2(1*H*)-pyridones as potential anticancer agents†

Diana Hurtado-Rodríguez,[a] Diana Becerra,[a] Hugo Rojas,[a] Jovanny A. Gómez Castaño,*[b] Mario A. Macías *[c] and Juan-Carlos Castillo *[a]

Received 22nd June 2024
Accepted 28th July 2024

DOI: 10.1039/d4ra04563g

rsc.li/rsc-advances

A series of 3-cyano-2(1*H*)-pyridones **4a–c** were efficiently synthesized using an expeditious microwave-assisted multicomponent approach. Single-crystal XRD analysis revealed the presence of six independent molecules in the asymmetric unit cell for all compounds, with the crystal packing stabilized by a network of cyclic dimers formed by N–H⋯O=C and C–H⋯O=C intermolecular interactions. Additional supramolecular interactions, including C–H⋯π, C–N⋯π, and π⋯π, and C–H⋯X (for halogenated derivatives, *i.e.*, **4b** and **4c**), appear crucial for crystal stabilization. Density Functional Theory (DFT) calculations were employed to understand the electronic structures and potential binding affinities. Comprehensive spectroscopic characterization by FT-IR, UV-Vis, NMR, and HMRS techniques confirmed the structures of all synthesized compounds. Differential scanning calorimetry (DSC) and thermogravimetric analysis (TGA) were employed to evaluate the thermal stability of these compounds. The *in vitro* anticancer activity was evaluated against a panel of 60 human cancer cell lines, demonstrating promising activity against non-small-cell lung and breast cancer cell lines. Notably, compounds **4a** and **4c** exhibited the highest anticancer activity against the HOP-92 and MCF7 cell lines, with growth inhibition percentages (GI%) of 54.35 and 40.25, respectively.

1. Introduction

2(1*H*)-Pyridone derivatives are six-membered aromatic N-heterocyclic compounds that incorporate carbonyl and amine functionality and have emerged as privileged scaffolds in medicinal chemistry. These molecules exhibit intriguing tautomeric behavior, predominantly existing as the lactam form (2(1*H*)-pyridone) due to its enhanced thermodynamic stability compared with the lactim form (2-hydroxypyridine) in both solid and solution states (Scheme 1).[1] 2(1*H*)-Pyridone derivatives possess a remarkable combination of physicochemical properties, including favorable metabolic stability, water solubility and balanced lipophilicity.[2–5] These characteristics, coupled with their ability to act as excellent hydrogen bond donors and acceptors, allow them to mimic nonpeptidic structures and effectively interact with biological targets.[2,5]

The properties of 2(1*H*)-pyridones have fueled their exploration in various pharmacological applications (Fig. 1). Naturally occurring examples, such as huperzine A employed for Alzheimer's treatment,[6] and fredericamycin A a promising anticancer lead,[7] showcase their inherent biological potential. The recent emergence of 2(1*H*)-pyridone derivatives in FDA-approved drugs further underscores their translational value.[8–10] Tazemetostat, a 2020-approved oral inhibitor of enhancer of zeste homolog 2 (EZH2), exemplifies this class.[11] Interestingly, its active pharmacophore is the 3-(aminomethyl)-pyridin-2(1*H*)-one moiety, strategically obtained *via* chemoselective reduction of a 3-cyano-2(1*H*)-pyridone precursor. It highlights the continued need for efficient synthetic strategies to access diverse 3-cyano-2(1*H*)-pyridone derivatives, paving the way for further exploration of their therapeutic potential in various diseases.

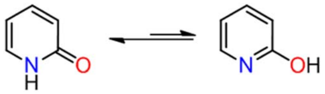

Scheme 1 Lactam–lactim tautomerization of 2(1*H*)-pyridone.

---

[a] *Grupo de Catálisis de la UPTC, Escuela de Ciencias Químicas, Universidad Pedagógica y Tecnológica de Colombia, Avenida Central del Norte 39-115, Tunja 150003, Colombia. E-mail: juan.castillo06@uptc.edu.co*

[b] *Grupo Química-Física Molecular y Modelamiento Computacional (QUIMOL), Escuela de Ciencias Químicas, Universidad Pedagógica y Tecnológica de Colombia, Avenida Central del Norte 39-115, Tunja 150003, Colombia. E-mail: jovanny.gomez@uptc.edu.co*

[c] *Cristalografía y Química de Materiales CrisQuimMat, Departamento de Química, Universidad de los Andes, Carrera 1 No. 18A-10, Bogotá 111711, Colombia. E-mail: ma.maciasl@uniandes.edu.co*

† Electronic supplementary information (ESI) available. CCDC 2335843–2335845. For ESI and crystallographic data in CIF or other electronic format see DOI: https://doi.org/10.1039/d4ra04563g

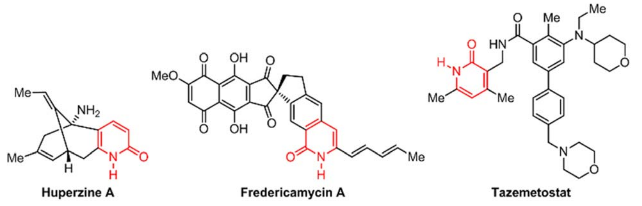

Fig. 1 Examples of bioactive 2(1*H*)-pyridone derivatives.

Traditional synthetic approaches for the preparation of 4,6-diaryl-3-cyano-2(1*H*)-pyridones often rely on a two-step sequence: (i) Michael-type addition involving enolate and α,β-unsaturated carbonyl acceptors, and (ii) subsequent oxidative intramolecular cyclization.[12–15] A diverse range of α,β-unsaturated carbonyl substrates have been effectively employed in this strategy, encompassing ethyl 2-cyano-3-arylacrylates,[12,13] 2-cyano-3-arylacrylamides,[14] and 1,3-diaryl-2-propen-1-ones.[15]

Multicomponent reactions (MCRs) have emerged as powerful tools for efficiently synthesizing diverse heterocyclic scaffolds, including aza-heterocycles.[16,17] However, the application of MCRs to prepare 4,6-diaryl-3-cyano-2(1*H*)-pyridones **4** remains relatively unexplored.[18–21] Pioneering work by Rong *et al.* described a three-component reaction for the synthesis of compounds **4** with good yields using malononitrile as the active methylene component and sodium hydroxide as the base under both grinding and conventional heating conditions (routes i and ii, Scheme 2a).[18,19] This approach was further extended by the same group, replacing malononitrile with cyanoacetamide as the active methylene compound for synthesizing analogous products with good yields (route iii, Scheme 2a).[20] El-Sayed *et al.* subsequently reported a solvent-free four-component reaction utilizing ethyl cyanoacetate as the active methylene compound and ammonium acetate (only 1 equivalent) acting dually as an ammonia surrogate and base, resulting in 4,6-diaryl-3-cyano-2(1*H*)-pyridones **4** with good yields (route iv, Scheme 2a).[21]

Despite reported synthetic procedures and spectroscopic characterization of 4,6-diaryl-3-cyano-2(1*H*)-pyridones **4a–c** (Scheme 2),[18–21] critical knowledge gap persists regarding their comprehensive physicochemical and biological properties. Notably, prior studies have not elucidated their crystal structure, performed detailed computational analysis using DFT, investigated their thermal behavior, or explored their potential as anticancer agents. This study meticulously addresses these shortcomings, offering a multifaceted exploration of compounds **4a–c**. Through a combination of crystallographic analysis, DFT calculations, thermal studies, and *in vitro* anticancer activity assays against a panel of 60 human cancer cell lines, we unveil valuable insights into their potential for future drug development endeavors.

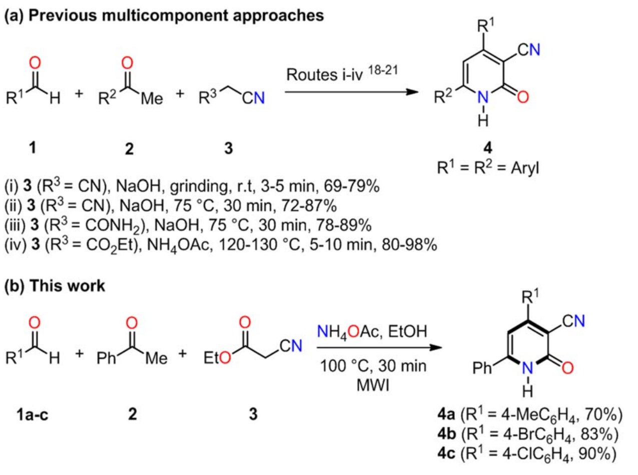

Scheme 2 Multicomponent approaches for the synthesis of 4,6-diaryl-3-cyano-2(1*H*)-pyridones **4**.

2. Results and discussion

2.1 Chemistry

Regrettably, our attempts to replicate the solvent-free MCR reported by El-Sayed *et al.*, to produce 4,6-diaryl-3-cyano-2(1*H*)-pyridone **4c** at temperatures ranging from 120 °C to 130 °C for 8 min, followed by crystallization in acetic acid, resulted in a yield lower than the reported 83%.[21] Therefore, we aimed to improve its efficiency by introducing two modifications: utilizing microwave heating and increasing the amount of ammonium acetate beyond 1 equivalent (Scheme 2b and Table 1). The optimization process evaluated the impact of temperature and reaction time, using 4-chlorobenzaldehyde **1c**, acetophenone **2**, ethyl cyanoacetate **3**, and excess ammonium acetate (3 equivalents) in ethanol (2 mL) under microwave irradiation (Table 1). Analysis of these parameters revealed that heating the reaction mixture at 100 °C for 30 min provided the optimal yield of **4c** (entry 1, Table 1). Furthermore, we successfully streamlined the purification process by leveraging the distinct solubility properties of **4c**. This approach facilitated

Table 1 Optimization of the microwave-assisted multicomponent synthesis of 3-cyano-2(1*H*)-pyridone **4c**

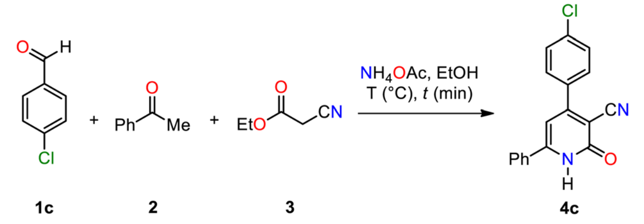

Entry[a]	Temperature (°C)	Time (min)	Yield **4c** (%)
1	100	30	90
2	120	30	89
3	150	30	61
4	100	15	77
5	100	5	42
6[b]	Reflux	300	29

[a] Reaction conditions: **1c** (3 mmol), **2** (3 mmol), **3** (3 mmol), NH_4OAc (9 mmol), EtOH (2 mL), 100–150 °C, 5–30 min, MWI. [b] Absence of microwave irradiation.

the isolation of the target compound in high yield (90%) without column chromatography purification. Using higher temperatures or shorter reaction times resulted in decreased yields of **4c** (entries 2–5, Table 1). For comparison, conventional refluxing of the reaction mixture in ethanol for 5 h afforded **4c** in a mere 29% (entry 6, Table 1). This stark contrast highlights the superiority of microwave irradiation, which enhances yields and significantly expedites reaction times. The optimized microwave-assisted MCR protocol was further applied to synthesize 3-cyano-2(1*H*)-pyridones **4a** and **4b** in 70% and 83% yields, respectively (Scheme 2b).

2.2 FT-IR and NMR spectroscopy studies

FT-IR spectroscopy analysis of the synthesized 4,6-diaryl-3-cyano-2(1*H*)-pyridones **4a–c**, revealed characteristic absorption bands consistent with their proposed structures (Scheme 2b). The N–H stretching vibration appeared in the range of 2800–3100 cm^{-1}, while the C≡N and C=O functionalities were identified by their respective stretching vibrations at 2217–2218 cm^{-1} and 1636–1639 cm^{-1}, respectively (Fig. S1–S3 in ESI†). Further structural elucidation was achieved using ^{1}H-NMR spectroscopy in DMSO-d_6 (Fig. S7, S12 and S17 in ESI†). A singlet observed at δ 6.79–6.84 ppm was assigned to the H-5 proton, and a broad singlet at δ 11.65–12.88 ppm corresponded to the exchangeable NH proton of the 2(1*H*)-pyridone ring. Analysis of the ^{13}C-NMR spectra (Fig. S8, S13 and S18 in ESI†), also recorded in DMSO-d_6 with extended acquisition times (up to 6 h), revealed a notable absence of signals for most quaternary carbons within the 2(1*H*)-pyridone ring. This phenomenon could be attributed to the dynamic equilibrium between lactam and lactim tautomers. While this equilibrium affects the detectability of carbons C-2 to C-6, the absence of signal duplication aligns with the predominant presence of the lactam form in the solution. Moreover, the ^{13}C-NMR spectra successfully confirmed the presence of C=O carbon (δ 161.7–162.5 ppm) and the C-5 carbon (δ 105.6–106.1 ppm) within the synthesized compounds.

2.3 UV-Vis spectroscopy and solvatochromic studies

UV-Vis spectroscopy was employed to investigate the electronic transitions of the synthesized compounds **4a–c**. Initial analyses were conducted in ethanol, a protic and polar solvent, at a concentration of 20 μM, with scans ranging from 200 to 500 nm (Fig. 2).

The UV-Vis spectra of compounds **4a–c** displayed three distinct absorption bands within the range of 217–275 nm (Table 2). These bands were attributed to various electronic transitions involving both n → π* and π → π* states. In addition, the spectra revealed two broad bands between 275 and 410 nm, which were assigned to the electronic transitions of the HOMO−1 ($\pi_{\mathrm{Ph(C)}}$) and HOMO (n_O) to LUMO ($\pi^*_{C=O}$) orbitals (Table 2). These specific assignments were achieved by a combined approach using vertical electronic and natural bond orbital (NBO) calculations at the B3LYP/6-311++G(2df,2dp) level of theory, in conjunction with previously reported spectra for structurally similar 4,6-diaryl-3-cyano-2(1*H*)-pyridones.[12]

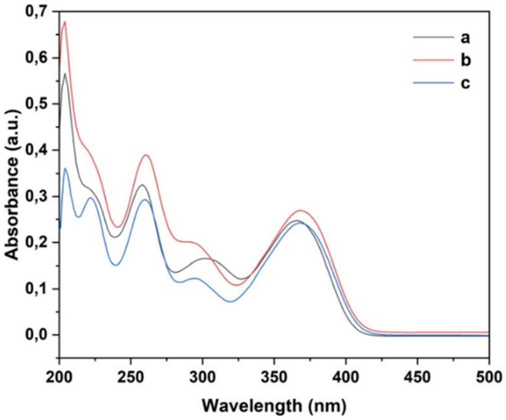

Fig. 2 UV-Vis spectra of compounds **4a** (R^1 = Me), **4b** (R^1 = Br), and **4c** (R^1 = Cl) in ethanol (20 μM).

The electronic absorption assignments observed, alongside FT-IR analysis, support the predominance of the lactam tautomeric form in both solution and solid states. This conclusion is further strengthened by the presence of C=O stretching vibrations in the FT-IR spectra (1636–1639 cm^{-1}) and the corresponding C=O carbon signals in the ^{13}C-NMR spectra (161.7–162.5 ppm) of compounds **4a–c.** The UV-Vis spectroscopy results, coupled with established insights into the lactam–lactim equilibrium, underscore the influence of solvent polarity in determining the predominant tautomeric form. The 2-hydroxypyridine tautomer **5** exhibits lower polarity than the lactam tautomer **4**, which can be attributed to the presence of a charge-separated mesomeric form **4′** for the lactam tautomer (Scheme 3).[12]

Consequently, electron-withdrawing substituents at positions 4 and 6 of the pyridine ring and polar protic solvents significantly stabilize the charge-separated resonance structure **4′**, favoring the more polar lactam form **4.** The lactam tautomer **4** achieves stability when exposed to polar protic solvents due to its ability to act as a hydrogen-bond donor to carbonyl oxygen. Conversely, the 2-hydroxypyridine tautomer **5** may gain some stabilization in solvents that primarily function as hydrogen-bond acceptors.[12] To gain further insight into the n → π* electronic transition of the C=O group associated with the lactam–lactim equilibrium in compounds **4a–c**, a solvatochromic study was undertaken using a range of polar solvents with varying dielectric constants (ε): ethanol ($\varepsilon = 24.5$), acetonitrile ($\varepsilon = 37.5$), and dimethylsulfoxide (DMSO, $\varepsilon = 46.7$). As illustrated in Fig. 3 and Table 2, all compounds displayed a moderate bathochromic shift (red shift) in the n → π* electronic transition of the C=O group with increasing solvent polarity. As mentioned earlier, this phenomenon can be attributed to the enhanced stabilization of the charge-separated mesomeric form **4′** with increasing solvent polarity (Scheme 3).

Furthermore, we investigated the influence of substituents at the 4-position of the aromatic ring on the electronic transitions. The presence of a more electronegative substituent (R^1 = Br and Cl) resulted in a bathochromic shift in the n → π* electronic

Table 2 Comparison between experimental (20 μM) and calculated (TD-DFT, B3LYP/6-311++g(2df,2pd)) UV-Vis electronic transitions of compounds **4a–c** in different solvents

		Experimental		Calculated						
Compound	Solvent	λ (nm)	$\varepsilon \times 10^4$ (L mol^{-1} cm^{-1})	λ (nm)	f	Normalized coefficient	Transition percentage	$\Delta\lambda$ (nm)	Transition	Assignment[a]
4a	EtOH	204	2.80	241.6	0.148	0.67332	90.7	−37.6	HOMO−1–LUMO+1	$\pi_{Ph(C)} - \pi^*_{Ph(B)}$
	EtOH	221	1.55	247.7	0.027	0.65845	86.7	−26.7	HOMO–LUMO+2	$n_O - \pi^*_{Ph(B)}$
	EtOH	257	1.60	263.0	0.212	0.68038	92.6	−6.0	HOMO–LUMO+1	$n_O - \pi^*_{Ph(B)}$
	EtOH	301	0.85	328.9	0.238	0.69747	97.3	−27.9	HOMO−1–LUMO	$\pi_{Ph(C)} - \pi^*_{C=O}$
	EtOH	365	1.20	357.4	0.493	0.69727	97.2	7.6	HOMO–LUMO	$n_O - \pi^*_{C=O}$
	ACN	369	1.40	357.1	0.493	0.69717	97.2	11.9	HOMO–LUMO	$n_O - \pi^*_{C=O}$
	DMSO	376	1.25	358.1	0.509	0.69725	97.2	17.9	HOMO–LUMO	$n_O - \pi^*_{C=O}$
4b	EtOH	203	3.40	242.6	0.001	0.69800	97.4	−39.6	HOMO−6–LUMO	$\pi_{Ph(C)} - \pi^*_{C=O}$
	EtOH	217	2.05	246.7	0.012	0.65984	87.1	−29.7	HOMO–LUMO+3	$n_O - \pi^*_{Ph(B)}$
	EtOH	260	1.95	264.6	0.194	0.68574	94.0	−4.6	HOMO–LUMO+1	$n_O - \pi^*_{Ph(C)}$
	EtOH	290	1.00	325.8	0.252	0.69615	96.9	−35.8	HOMO−1–LUMO	$\pi_{Ph(C)} - \pi^*_{C=O}$
	EtOH	368	1.35	360.9	0.515	0.69817	97.5	7.1	HOMO–LUMO	$n_O - \pi^*_{C=O}$
	ACN	372	1.40	360.6	0.514	0.69814	97.5	11.4	HOMO–LUMO	$n_O - \pi^*_{C=O}$
	DMSO	378	1.25	361.6	0.530	0.69830	97.5	16.4	HOMO–LUMO	$n_O - \pi^*_{C=O}$
4c	EtOH	204	1.80	239.5	0.031	0.51929	53.9	−35.5	HOMO−1–LUMO+2	$\pi_{Ph(C)} - \pi^*_{Ph(B)}$
	EtOH	222	1.48	246.9	0.011	0.65532	85.9	−24.9	HOMO–LUMO+3	$n_O - \pi^*_{Ph(B)}$
	EtOH	259	1.46	267.8	0.221	0.68072	92.7	−8.8	HOMO–LUMO+1	$n_O - \pi^*_{Ph(C)}$
	EtOH	295	0.60	320.3	0.246	0.69833	97.5	−25.3	HOMO−1–LUMO	$\pi_{Ph(C)} - \pi^*_{C=O}$
	EtOH	368	1.21	360.4	0.489	0.69941	97.8	7.6	HOMO–LUMO	$n_O - \pi^*_{C=O}$
	ACN	372	1.33	360.2	0.489	0.69938	97.8	11.8	HOMO–LUMO	$n_O - \pi^*_{C=O}$
	DMSO	380	1.06	361.1	0.504	0.69954	97.9	18.9	HOMO–LUMO	$n_O - \pi^*_{C=O}$

[a] For ring labeling (*i.e.*, A, B or C), see Fig. 5.

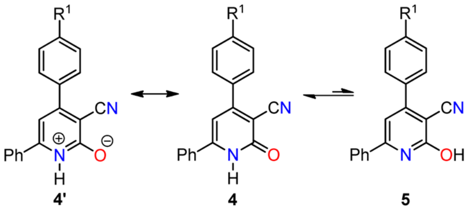

Scheme 3 Influence of mesomeric form **4′** on the lactam–lactim tautomeric equilibrium in 4,6-diaryl-3-cyano-2(1*H*)-pyridones.

transition from the HOMO to LUMO orbitals. This observation reveals a correlation between the bathochromic shift and a reduction in the band gap for compounds containing electron-withdrawing substituents (R^1 = Br and Cl), which contrasts with the behavior observed for the compound containing an electron-donating group (R^1 = Me). While Fig. 3 reveals that compounds **4a–c** exhibited their highest absorbance in acetonitrile, interestingly, the n → π* electronic transition displayed a hypochromic effect in DMSO. This observation indicates that the electron-withdrawing substituent (Cl in compound **4c**) reduces the absorbance (1.06×10^4 L mol^{-1} cm^{-1}), which contrasts with the slightly higher absorbance observed for the compound containing an electron-donating substituent (CH_3 in compound **4a**, 1.25×10^4 L mol^{-1} cm^{-1}).

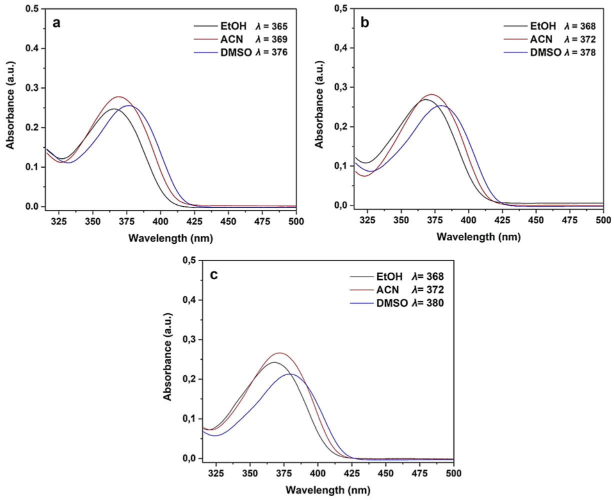

Fig. 3 UV-Vis spectra and solvatochromic study of compounds **4a** (R^1 = Me), **4b** (R^1 = Br), and **4c** (R^1 = Cl).

2.4 Frontier molecular orbital analysis and molecular reactivity

Frontier Molecular Orbital (FMO) analysis was performed to elucidate the reactivity and chemical stability trends of compounds **4a–c**. The HOMO is primarily localized on the

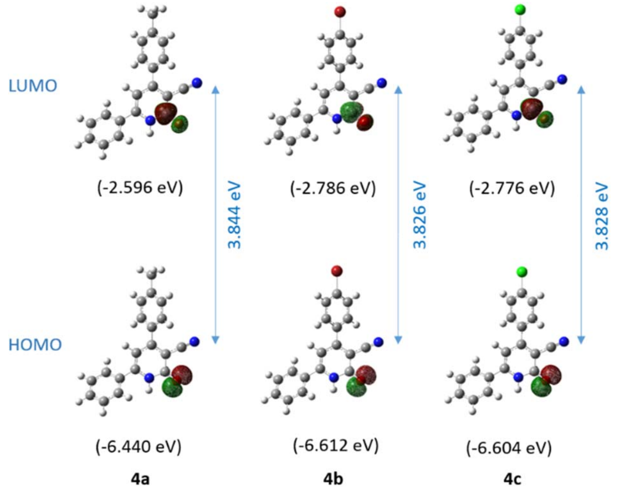

Fig. 4 Calculated frontier molecular orbitals (HOMO and LUMO) and band gap of compounds **4a–c** using the B3LYP/6-311++G(2df,2pd) approximation level.

oxygen atom of the carbonyl group, while the LUMO is located on the antibonding π* orbital of the same carbonyl group (Fig. 4). These findings are consistent with the previously proposed charge-separated mesomeric form **4'** and its corresponding resonance structure, the lactam tautomer **4** (Scheme 3). The calculated HOMO stabilization energies for compounds **4a**, **4b**, and **4c** were 6.44, 6.61, and 6.60 eV, respectively. Similarly, the LUMO energies were 2.60, 2.79, and 2.78 eV, respectively. The HOMO–LUMO energy gaps for compounds **4a**, **4b**, and **4c** were calculated to be 3.84, 3.83, and 3.83 eV, respectively. These results indicate a notable level of chemical stability and reduced reactivity attributable to the enhanced stability of the electron cloud.

Table 3 presents the calculated global reactivity descriptors for compounds **4a–c**, including ionization potential (IP), electron affinity (EA), electrophilicity index (ω), chemical potential (μ), electronegativity (χ), and hardness (η). Koopmans' theorem establishes a correlation between the HOMO and LUMO energy levels of a molecule and its IP and EA, respectively.[22] Electronegativity (χ) is calculated as the average of the HOMO and LUMO energies using the equation $\chi = (\mathrm{IP} + \mathrm{EA})/2$.[23] Hardness ($\eta$), a valuable indicator of chemical stability, is inversely proportional to the HOMO–LUMO energy gap.[24,25] Parr *et al.* introduced the electrophilicity index (ω) defined as $\omega = \mu^2/2\eta$, where μ is the chemical potential calculated as $\mu = -(\mathrm{IP} + \mathrm{EA})/2$.[26]

Table 3 HOMO/LUMO energies (eV) and global reactivity descriptors (eV) for compounds **4a–c**

Parameters	4a	4b	4c
HOMO energy	−6.440	−6.612	−6.604
LUMO energy	−2.596	−2.786	−2.776
HOMO–LUMO energy gap	3.844	3.826	3.828
Ionization potential (IP)	6.440	6.612	6.604
Electron affinity (EA)	2.596	2.786	2.776
Electrophilicity index (ω)	2.655	2.886	2.873
Chemical potential (μ)	−4.518	−4.699	−4.690
Electronegativity (χ)	4.518	4.699	4.690
Hardness (η)	3.844	3.826	3.828

Table 4 Dihedral angles (°) A–B and A–C for each independent molecule in compounds **4a–c**

Dihedral angles (°)	4a	4b	4c
A–B	26.8(19)	23.0(3)	27.6(13)
	32.2(18)	24.1(3)	23.1(14)
	30.1(18)	27.7(3)	28.2(14)
	32.0(19)	28.5(2)	23.9(13)
	27.2(19)	27.4(3)	27.9(13)
	29.7(17)	28.4(3)	26.8(13)
A–C	53.0(2)	49.7(3)	59.0(14)
	57.2(2)	48.3(3)	52.1(15)
	48.3(2)	46.2(3)	58.9(14)
	57.8(2)	47.1(3)	49.3(15)
	53.9(2)	58.5(3)	46.1(13)
	49.3(2)	57.3(3)	45.6(15)

The calculated electrophilicity index values for **4a** (2.66 eV), **4b** (2.89 eV), and **4c** (2.87 eV) denote moderate electrophilicity toward electron-rich species (Table 3). The chemical potential values (μ) for **4a** (−4.52 eV), **4b** (−4.70 eV), and **4c** (−4.69 eV) imply a moderate ability to attract electrons. The electronegativity values (χ) follow the same trend, ranging from 4.52 to 4.70 eV. The high hardness values (η) calculated from the HOMO–LUMO energy gap ranging from 3.83 to 3.84 eV denote significant resistance to electron transfer for all compounds, resulting in reduced chemical reactivity.

2.5 Crystalline structural analysis

2.5.1. Single-crystal X-ray diffraction. Single-crystal X-ray diffraction analysis was performed to definitively determine the molecular structures of compounds **4a–c** in the solid state. A search for structural analogs within the Cambridge Structural Database (CSD) version 5.45 (accessed June 2024) using

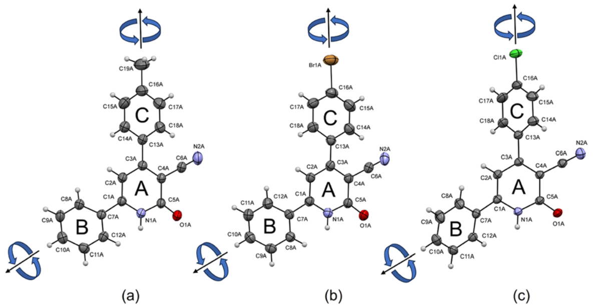

Fig. 5 Molecular structures of compounds (a) **4a**, (b) **4b**, and (c) **4c** show anisotropic thermal vibrations. The ellipsoids represent a 30% probability level, and hydrogen atoms are depicted as spheres with arbitrary radii. Blue arrows denote the free rotation between C7A–C1A and C3A–C13A atoms, resulting in six independent molecules in the asymmetric unit for **4a–c**. The dihedral angles between the planes containing rings A–B and A–C for compounds **4a–c** were measured using Mercury software (Fig. 4 and Table 4).[27]

ConQuest software version 2024.1.0 yielded no prior crystallographic reports for molecules containing identical core structures. Fig. 5 presents the molecular representations of compounds **4a–c** as ellipsoid models with 30% probability level. Notably, the unit cell volumes for all three compounds exhibit high values (Table S5 in ESI†). This observation can be attributed to the six independent molecules within the asymmetric units of their respective crystal structures. This packing arrangement likely arises from the inherent rotational flexibility of the C–C bonds connecting the aromatic rings, with bond distances characteristic of single C–C bonds (approximately 1.4–1.5 Å). This observed lack of planarity in the molecular conformations, along with the single-bond character of the inter-ring C–C bonds, supports the conclusion of minimal resonance interactions between the aromatic fragments.

Further analysis of the crystal structures of compounds **4a–c** revealed the presence of various intermolecular interactions that govern their solid-state packing arrangements (Fig. 6 and Table 5). Independent of the conformational orientation of individual molecules, inversion symmetry-related molecules are linked through a combination of N–H⋯O and C–H⋯O hydrogen bonds. Notably, some of these hydrogen bonds exhibit a split character, where a single oxygen atom acts as a hydrogen bond acceptor for two (N,C)–H donors. As expected, N–H⋯O hydrogen bonds display shorter distances compared to C–H⋯O interactions due to the enhanced acidity of the N–H proton.

The observed free rotation around the C7A–C1A and C3A–C13A bonds, leading to six independent molecules within the asymmetric units of **4a–c**, is influenced by packing constraints. Interestingly, the formation of precisely six distinct conformers in each crystal structure is associated with the development of directional molecular chains extending along the [100], [010], and [100] crystallographic directions for **4a**, **4b**, and **4c**,

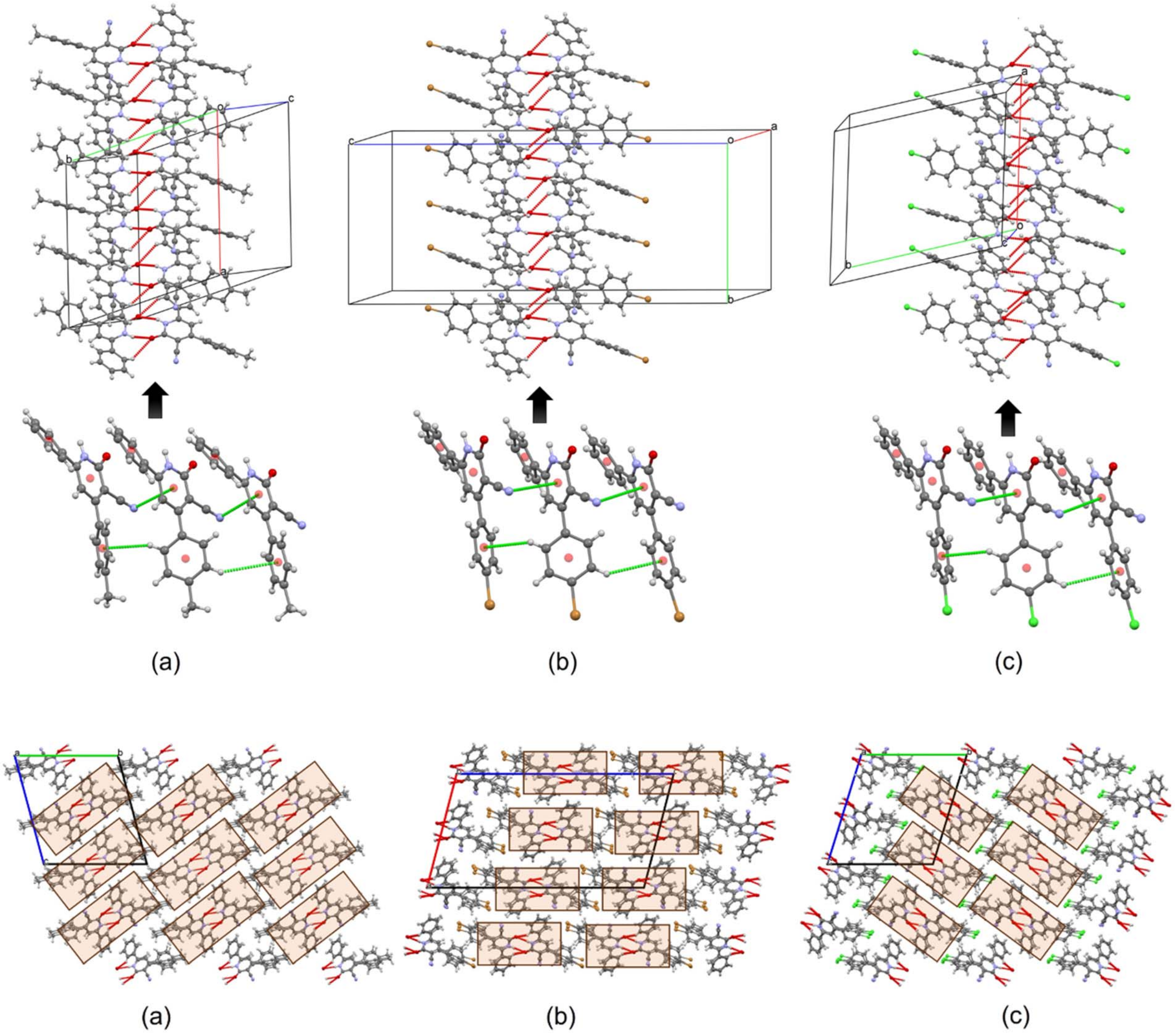

Fig. 6 Molecular chains formed by dimers of inversion-related molecules connected by N–H⋯O, C–H⋯O, C–H⋯π, C–N⋯π, and π⋯π interactions for compounds (a) **4a**, (b) **4b**, and (c) **4c**. Brown and green spheres correspond to Br and Cl atoms, respectively. Crystal structures of compounds (a) **4a**, (b) **4b**, and (c) **4c**, showing the molecular packings.

Table 5 Selected hydrogen-bond geometry (Å, °) for compounds **4a–c**

D–H···A	D–H	H···A	D···A	D–H···A	Symmetry code
Compound 4a					
N1A–H1A···O1D	0.86	1.99	2.817(4)	161	$1-x,1-y,-z$
N1B–H1B···O1F	0.86	1.99	2.800(4)	165	x,y,z
N1C–H1C···O1C	0.86	1.99	2.788(4)	161	$1-x,1-y,-z$
N1D–H1D···O1A	0.86	1.99	2.827(4)	164	$1-x,1-y,-z$
N1E–H1E···O1E	0.86	2.00	2.819(4)	158	$-x,1-y,1-z$
N1F–H1F···O1B	0.86	1.96	2.803(4)	165	x,y,z
C8C–H8C···O1C	0.93	2.57	3.189(4)	125	$1-x,1-y,-z$
C8D–H8D···O1A	0.93	2.57	3.202(4)	126	$1-x,1-y,-z$
C8F–H8F···O1B	0.93	2.55	3.205(4)	128	x,y,z
Compound 4b					
N1A–H1A···O1A	0.86	1.98	2.797(6)	158	$1-x,-y,1-z$
N1B–H1B···O1C	0.86	1.97	2.812(6)	166	$1-x,1-y,1-z$
N1C–H1C···O1B	0.86	1.98	2.815(5)	164	$1-x,1-y,1-z$
N1D–H1D···O1E	0.86	1.97	2.806(6)	165	$-x,1-y,1-z$
N1E–H1E···O1D	0.86	2.01	2.834(6)	161	$-x,1-y,1-z$
N1F–H1F···O1F	0.86	1.95	2.781(5)	163	$-x,1-y,1-z$
C8A–H8A···O1A	0.93	2.53	3.215(7)	130	$1-x,-y,1-z$
C8B–H8B···O1C	0.93	2.52	3.214(6)	132	$1-x,1-y,1-z$
C8C–H8C···O1B	0.93	2.45	3.148(7)	132	$1-x,1-y,1-z$
C8D–H8D···O1E	0.93	2.49	3.167(7)	130	$-x,1-y,1-z$
C8F–H8F···O1F	0.93	2.49	3.159(7)	129	$-x,1-y,1-z$
Compound 4c					
N1A–H1A···O1C	0.86	1.97	2.816(3)	166	$x,1+y,z$
N1B–H1B···O1B	0.86	1.99	2.809(3)	158	$1-x,2-y,1-z$
N1C–H1C···O1A	0.86	1.97	2.815(3)	165	$x,-1+y,z$
N1D–H1D···O1F	0.86	1.99	2.827(3)	165	$1-x,-y,-z$
N1E–H1E···O1E	0.86	1.94	2.777(3)	163	$-x,-y,-z$
N1F–H1F···O1D	0.86	2.00	2.830(3)	162	$1-x,-y,-z$
C8E–H8E···O1E	0.93	2.48	3.159(3)	130	$-x,-y,-z$

respectively. Within these chains, the 4-substituted aromatic rings (4-MeC_6H_4, 4-BrC_6H_4, and 4-ClC_6H_4) adopt conformations that favor the formation of C–H···π interactions, with H···π distances of approximately 2.9 Å, contributing to the overall structural stability (Fig. 6). Furthermore, unconventional C–N···π contacts (N···π distances ranging from 3.4 to 3.6 Å) participate in the assembling of supramolecular chains by facilitating the appropriate molecular orientations necessary for the formation of weak π···π interactions.

From a supramolecular perspective, the crystal structures of compounds **4a–c** can be envisioned as assemblies of structurally similar molecular chains, resembling supramolecular bricks (Fig. 6). In compound **4a**, these bricks are connected primarily through weak C–H···π interactions and van der Waals forces. In contrast, the packing arrangement in compounds **4b** and **4c** involves additional intermolecular C–H···Cl and C–H···Br halogen bonding interactions, with H···Cl and H···Br distances ranging from 2.8 to 3.1 Å. Furthermore, C–H···N–C interactions involving the cyano group (CN), with H···N distances of approximately 2.9 Å, contribute to the interconnection of the chains (Fig. 6). It is noteworthy that despite the variation in the 4-substituent on the aromatic ring (4-MeC_6H_4, 4-BrC_6H_4, and 4-ClC_6H_4), the intermolecular interactions governing the assembly between the molecular chains exhibit a high degree of similarity across compounds **4a–c**.

2.5.2. Topological study on electron density (*ρ*). To further explore the electronic properties of the main noncovalent interactions that regulate the crystalline assembly of compounds **4a–c**, a topological analysis was performed on the gradient vector field of the electron density ($\nabla\rho$) using the QTAIM-C developed by Richard Bader and colleagues.

As previously mentioned, the carbonyl oxygen atom in compounds **4a–c** appears to be crucial for the stability of these crystalline systems. It forms two simultaneous hydrogen bonds: one with the amine's hydrogen and another with aromatic hydrogen from a symmetrically related molecular unit (Fig. 6 and 7-top). To test this hypothesis, we performed QTAIM-C analysis on the unmodified structure of the corresponding dimer extracted from these crystal systems. As shown in Fig. 7-bottom, the topological analysis revealed the presence of two bond critical points (BCPs) and two corresponding bond paths (BPs) connecting each carbonyl oxygen atom with the hydrogen atoms involved in these hydrogen bonding interactions. The topological characterization of these BCPs, such as $\rho(r)$ and $\nabla^2\rho(r)$, confirms the presence of closed-shell hydrogen bonding interactions, which is consistent with the structural analysis observations. The electron density (ρ) at the BCPs indicates the strength of these interactions, with a higher electron density corresponding to stronger hydrogen bonding. Electron density values at BCPs of the type C=O···H–Ph HB ranged from 0.007 to 0.009 au in the three systems, indicating weak-to-moderate strength hydrogen bonding interactions ($0.002 \leq \rho \leq 0.4$ au, for neutral systems).[28] As shown in Fig. 7, dimer **4a** exhibited slightly lower electronic density values for these types of BCPs compared to **4b** and **4c**. On the other hand, the calculated electron density at the C=O···H–N BCPs attained values of 0.025 au for system **4a** and 0.024 au for systems **4b** and **4c**, revealing stronger bidirectional dimer interactions between the carbonyl oxygen atom and the amine hydrogen in compounds **4a–c**. These findings suggest that a carbonyl oxygen atom in compounds **4a–c** is critical for stable crystalline assemblies.

Our topological analysis unexpectedly revealed a long intermolecular C≡N···H–C bond path (approximately 7.97 au) in halogenated dimers **4b** and **4c**, connecting the cyano group with an aromatic hydrogen atom from a neighboring molecule (Fig. 7-bottom). The electron densities at these BCPs reached low values of approximately 3.7×10^{-4} au, suggesting weak but potentially significant dispersive interactions contributing to the overall supramolecular organization observed in these molecular crystals. In addition, relatively high ellipticities ($\varepsilon \approx 2.2$) were observed on these BCPs, indicating that these interactions exhibit partial π-character. The absence of intermolecular C≡N···H–C interactions in compound **4a** suggests that the introduction of halogen atoms in compounds **4b** and **4c** promotes the formation of weak non-covalent interactions, which may play an auxiliary role in stabilizing the molecular packing arrangements.

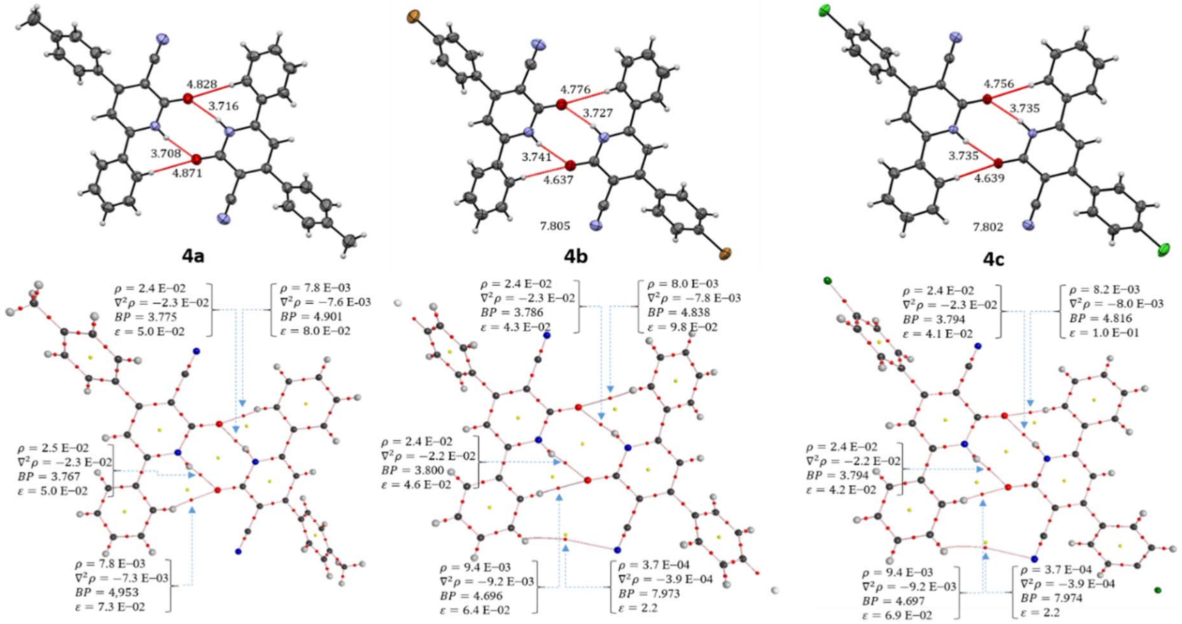

Fig. 7 Dimeric interaction projected from the crystal structures of compounds **4a–c** (top) *vs.* the corresponding critical points (CPs) analysis on the electron density performed using the QTAIM (bottom). Bond paths (pink lines), BCPs (red dots), and RCPs (yellow dots). Electron density (ρ), Laplacian ($\nabla^2\rho$), and length of contact distances and bond paths (BP) are expressed in atomic units (au).

2.5.3. Hirshfeld surface analysis.

Hirshfeld surface (HS) analysis was employed to investigate the intermolecular interactions governing the crystal packing of compounds **4a–c**. HS mapped over normalized contact distance (d_{norm}) representing the distance from a point on the surface to the nearest atom inside (d_i) or outside (d_e) the surface. These calculations were performed using CrystalExplorer software.[29,30] Analysis of d_{norm} allows for the visualization of close contacts and hydrogen bonds through color-coded maps, where red regions signify distances shorter than the sum of van der Waals (vdW) radii, white regions represent distances close to the vdW sum, and blue regions indicate distances exceeding the vdW sum. Fig. 8. The prominent red spots on the HS maps of all compounds correspond to the strong N–H···O and C–H···O hydrogen bonds connecting inversion-related molecules.

The two-dimensional (2D) fingerprint plots in Fig. 8 depict the contributions of various interatomic contacts to the overall HS for each compound. A qualitative comparison of these plots reveals similar patterns for compounds **4b** and **4c**, which differ from those observed for **4a**. These differences can be attributed

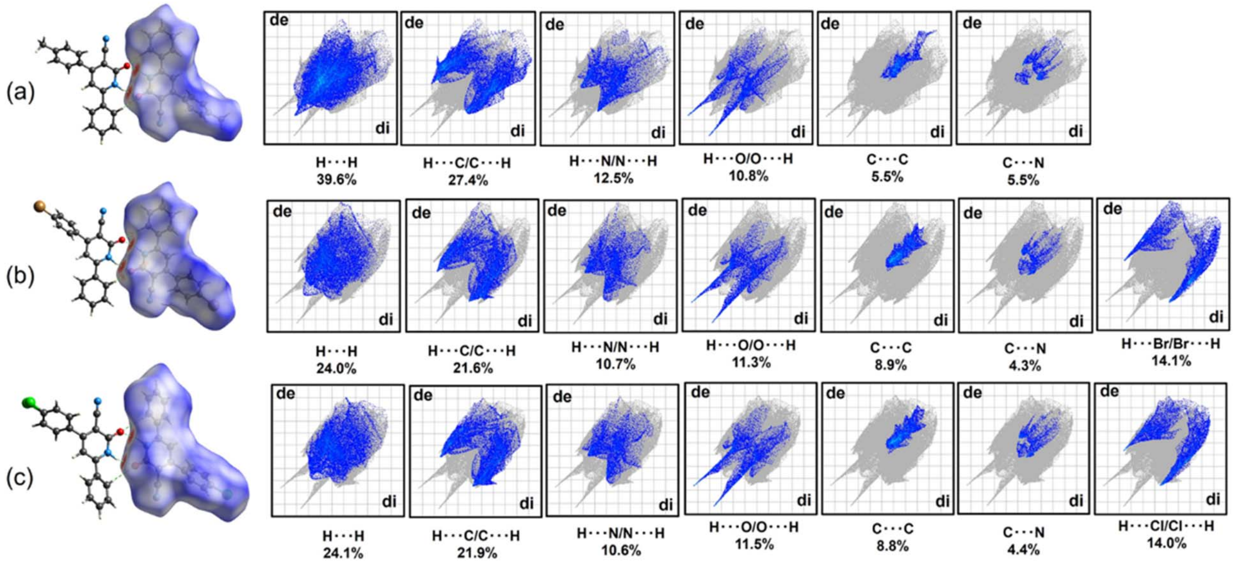

Fig. 8 Hirshfeld surfaces mapped over d_{norm} and 2D fingerprint plots including relative contributions (%) to the Hirshfeld surface area for the various close intermolecular contacts in compounds (a) **4a**, (b) **4b**, and (c) **4c**.

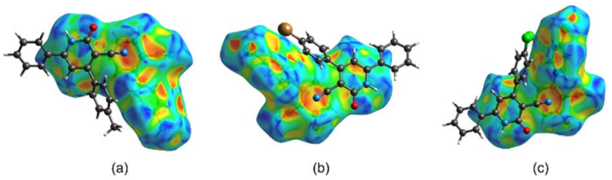
(a) (b) (c)

Fig. 9 Hirshfeld surfaces mapped with shape index showing the hollows (red) on the aromatic rings due to C–N⋯π contacts in compounds (a) **4a**, (b) **4b**, and (c) **4c**.

to the varying 4-substituents on the aromatic ring C (4-MeC$_6$H$_4$, 4-BrC$_6$H$_4$, and 4-ClC$_6$H$_4$), which influence the formation of intermolecular contacts. In all compounds, H⋯H interactions represent the most significant contribution of the HS maps, with the highest percentage observed for compound **4a**, as expected. The presence of 4-BrC$_6$H$_4$ and 4-ClC$_6$H$_4$ fragments in compounds **4b** and **4c** leads to a notable contribution from C–H⋯(Br, Cl) interactions (14.1% and 14.0% for **4b** and **4c**, respectively), highlighting the importance of these interactions in stabilizing the crystal packing.

Beyond the conventional N–H⋯O, C–H⋯O hydrogen bonds, C–H⋯π and π⋯π interactions, HS analysis revealed the presence of additional, potentially weak C–N⋯π contacts relevant to the supramolecular assembly in all compounds. These C–N⋯π contacts contribute approximately 4.3–5.5% to the total HS map for each compound. Fig. 9 presents the shape index maps, emphasizing the distribution of these C–N⋯π contacts. The presence of red hollows on the shape index maps indicates areas where the surfaces around C–N fragments come into proximity with the surfaces of the aromatic rings in each compound. These hollows, centered on the centroids of the π-systems, further support the existence of these weak C–N⋯π contacts (N⋯π distances: 3.4–3.6 Å).

2.6 UV-Vis diffuse reflectance

UV-Vis diffuse reflectance spectroscopy was used to measure the absorption characteristics of compounds **4a–c** (Fig. 10). The estimated absorption wavelengths for these compounds were approximately 350 and 400 nm. Compounds containing electron-withdrawing groups (R^1 = Br and Cl) showed higher absorption intensity than those containing an electron-donating group (R^1 = Me). The band gap energies of compounds **4a–c** were determined by extrapolating the Tauc plot, where the curve intersects the *y*-axis, assuming a direct band gap. The estimated band gap energies were 2.69, 2.71, and 2.74 eV for compounds **4a**, **4b**, and **4c**, respectively (Fig. 11). However, the band gap energies for compounds **4a**, **4b**, and **4c** were determined to be 3.844, 3.826, and 3.828 eV, respectively, using the B3LYP/6-311++G(2df,2pd) approximation level. In the gas phase, the absence of stabilizing interactions can lead to higher energy transitions, resulting in elevated band gap values. In summary, the disparity between the band gap values obtained from the Tauc plot and those calculated using the DFT method arises from fundamental differences in phase (solid *versus* gas), methodological approaches (empirical *versus* theoretical), and environmental effects (presence *versus* absence of intermolecular interactions). These factors collectively contribute to the observed differences in the band gap energies for compounds **4a–c**.

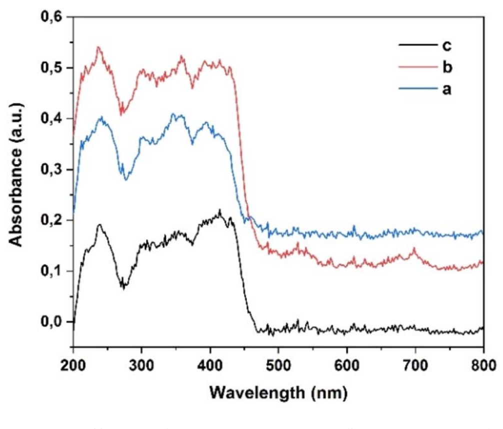

Fig. 10 UV-Vis diffuse reflectance spectra of compounds **4a–c**.

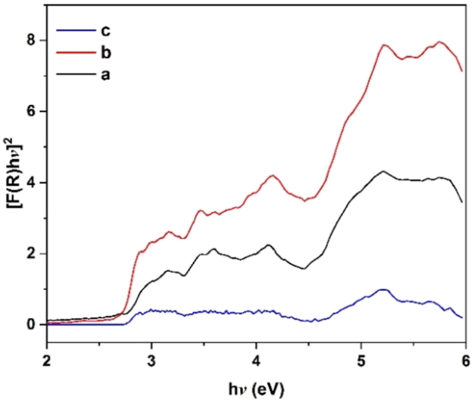

Fig. 11 Band gap values assessed by a correlated curve of $(F(R)h\nu)^2$ set against photon energy plots of compounds **4a–c**.

2.7 Thermal analysis

Thermogravimetric analysis (TGA) and differential scanning calorimetry (DSC) were employed to evaluate the thermal

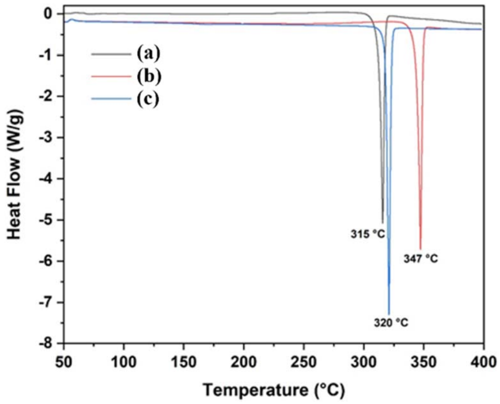

Fig. 12 TG thermograms of compounds **4a** (R^1 = Me), **4b** (R^1 = Br), and **4c** (R^1 = Cl).

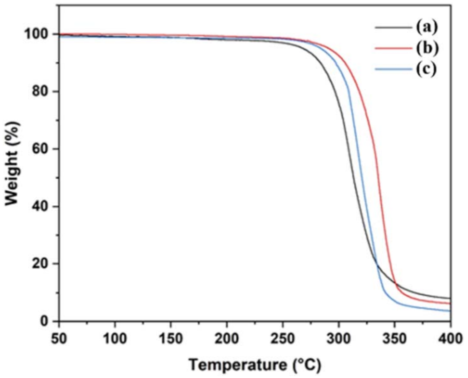

Fig. 13 DSC thermograms of compounds **4a** (R^1 = Me), **4b** (R^1 = Br), and **4c** (R^1 = Cl).

stability of compounds **4a–c**. TGA and DSC thermograms for each compound were recorded separately under a controlled nitrogen atmosphere using a heating rate of 10 °C min^{-1} and a continuous nitrogen flow of 25 mL min^{-1} over a temperature range of 25 to 400 °C (Fig. 12 and 13).

Analysis of the combined TGA and DSC thermograms for compound **4a** (R^1 = Me) revealed a melting process within the temperature range of 292–331 °C, characterized by a distinct endothermic peak at 315 °C (ΔH_{fus} = 117 J g^{-1}). Similarly, the TGA and DSC curves for compounds **4b** (R^1 = Br) and **4c** (R^1 = Cl) displayed analogous melting transitions within 321–348 °C and 303–337 °C, respectively. These melting processes were accompanied by prominent endothermic peaks observed at 347 °C (ΔH_{fus} = 125 J g^{-1}) for compound **4b** and 320 °C (ΔH_{fus} = 132 J g^{-1}) for compound **4c**.

The introduction of halogen substituents (Br and Cl) into compounds **4b** and **4c** appears to result in a slight increase in the enthalpy of fusion and the melting temperature range compared to compound **4a**. This observed trend can be attributed to stronger intermolecular interactions facilitated by halogen incorporation. As evidenced by single-crystal X-ray diffraction analysis (Section 2.5.1), these stronger interactions likely involve C–H⋯Cl and C–H⋯Br hydrogen bonding.

2.8 Anticancer studies

The *in vitro* anticancer activity of the synthesized 3-cyano-2(1*H*)-pyridones **4a–c** was evaluated against a panel of 60 human cancer cell lines, including leukemia, melanoma, lung, colon, central nervous system, ovarian, renal, prostate, and breast cancers. The National Cancer Institute (NCI) performed the evaluation using a single-dose treatment of 10 μM. Compounds **4a**, **4b**, and **4c** were assigned unique identifiers D-837648/1, D-837640/1, and D-829750/1, respectively, by the NCI. Detailed results, including the mean growth percentage (mean *G*%) and growth inhibition percentage (GI%) of treated cells relative to untreated controls, are depicted in Tables S2–S4.†[31,32] Table 6 summarizes the top five most promising findings, highlighting the highest GI% exhibited by compounds **4a–c** against various human cancer cell lines.

Table 6 Anticancer activity of 3-cyano-2(1*H*)-pyridones **4a–c**

Compound	Most sensitive cell lines	GI[a] (%)
4a	HOP-92 (non-small cell lung cancer)	54.35
	HCT-15 (colon cancer)	28.96
	UO-31 (renal cancer)	26.78
	SR (leukemia)	26.72
	T-47D (breast cancer)	26.54
4b	MCF7 (breast cancer)	24.72
	HOP-92 (non-small cell lung cancer)	23.42
	RPMI-8226 (leukemia)	23.33
	MOLT-4 (leukemia)	22.34
	NCI-H522 (non-small cell lung cancer)	21.22
4c	MCF7 (breast cancer)	40.25
	HOP-92 (non-small cell lung cancer)	31.79
	T-47D (breast cancer)	29.86
	UO-31 (renal cancer)	28.23
	UACC-62 (melanoma)	28.18

[a] GI% = 100 − *G*%.

The 3-cyano-2(1*H*)-pyridones **4a** and **4c** exhibited the most promising *in vitro* anticancer activity. These compounds displayed significant growth inhibition percentages (GI%) against the HOP-92 non-small-cell lung (54.35 for **4a**) and MCF7 (40.25 for **4c**) breast cancer cell lines. In addition, compounds **4b** and **4c** demonstrated moderate activity against the HOP-92 cell line with GI% values of 23.42 and 31.79, respectively. Conversely, compounds **4a** and **4b** showed low activity against the T-47D and MCF7 breast cancer cell lines, with GI% values of 26.54 and 24.72, respectively. Likewise, compounds **4a** and **4c** demonstrated low activity against the UO-31 renal cancer cell line, with GI% values of 26.78 and 28.23, respectively.

Interestingly, some studies have documented the anticancer activity of 2(1*H*)-pyridone derivatives against the MCF7 breast cancer cell line,[33–36] highlighting the 4-aryl-6-[benzo[*f*]coumarin-3-yl]-3-cyano-2(1*H*)-pyridones with GI_{50} values ranging from 0.003 to >50 μM, as well as 3,4,6-triaryl-2(1*H*)-pyridones exhibiting higher anticancer activity than the standard drug Nolvadex.[34,35] Conversely, limited data exists regarding their efficacy against HOP-92 and UO-31 cancer cell lines. Overall, the promising *in vitro* anticancer activity of compounds **4a–c** against the HOP-92 non-small-cell lung and breast cancer cell lines can be attributed to the presence of the 2(1*H*)-pyridone scaffold, aligning with findings on the antiproliferative properties of 2-pyridone derivatives.[33–36] However, further investigation is warranted to elucidate the underlying mechanisms of action of these compounds and to explore their potential for development as potential anticancer agents.

3. Conclusions

This study presents the multicomponent synthesis, spectroscopic characterization, crystallographic analysis, theoretical investigation, and initial evaluation of the anticancer activity of 4,6-diaryl-3-cyano-2(1*H*)-pyridones **4a–c**. The microwave-assisted protocol furnished the target compounds with good yields. This approach is notable for its simplicity of operation, use of an eco-friendly solvent, straightforward purification process, and simultaneous formation of four chemical bonds in a single step. The structures of **4a–c** were confirmed using various analytical techniques (FT-IR, UV-Vis, NMR, HRMS, TG, and DSC) and single-crystal X-ray diffraction analysis.

Density functional theory (DFT) calculations at the B3LYP/6-311++G(2df,2pd) level of theory were employed to optimize the molecular geometries of **4a–c** in the gas phase and various *in silico* solvent environments (ethanol, acetonitrile, and DMSO). Time-dependent DFT (TD-DFT) calculations provided insights into the electronic transitions responsible for the UV-Vis spectral bands. Natural bond orbital (NBO) population analysis yielded the frontier molecular orbital surfaces.

The topological analysis of the electron density, conducted using the QTAIM-C approach, highlighted the crucial role of the carbonyl oxygen atom in forming strong bidirectional hydrogen bonding interactions, primarily with the amine hydrogen and secondarily with aromatic hydrogens from neighboring molecules. Furthermore, the analysis revealed the presence of weak intermolecular $C{\equiv}N\cdots H{-}C$ contacts in the halogenated compounds **4b** and **4c**, which may contribute to the overall stability of the supramolecular assemblies. Hirshfeld surface analysis offered a quantitative and visual representation of these close contacts in real space, providing valuable insights into the nature of the noncovalent interactions that govern the crystalline packing of the 3-cyano-2(1*H*)-pyridones. These findings can be further utilized to design and synthesize new functional materials with specific properties.

Initial assessment of anticancer activity revealed that all compounds exhibited moderate cytotoxicity against human lung carcinoma (A549) and breast adenocarcinoma (MCF7) cell lines. Compounds **4a** and **4c** exhibited the most significant anticancer activity against HOP-92 non-small-cell lung and MCF7 breast cancer cell lines, with growth inhibition percentages (GI%) of 54.35 and 40.25, respectively. Further studies are needed to elucidate their mechanisms of action and enhance the anticancer potential of other 3-cyano-2(1*H*)-pyridones.

4. Experimental

4.1 Materials and methods

All chemical reactions were performed under a dry nitrogen atmosphere using oven-dried glassware. The reaction progress was monitored by thin-layer chromatography (TLC) on precoated silica gel (Merck Kieselgel 60 F254). Visualization was achieved using UV light at 254 and 365 nm. Solvents and commercially available reagents were purchased from Sigma-Aldrich and used without further purification unless otherwise stated. Microwave-assisted reactions were conducted using an Anton Paar Monowave 400 microwave reactor with 10 mL glass reaction vials (G30). Infrared spectra were recorded using a Thermo Scientific Nicolet 1550 Infrared spectrophotometer. ^{1}H and ^{13}C NMR spectra were acquired on a Bruker Avance 400 MHz spectrometer (for compounds **4a** and **4c**) and a Varian UNITYPLUS 500 MHz spectrometer (for compound **4b**), using deuterated dimethylsulfoxide (DMSO-d_6). Chemical shifts (δ) are reported in ppm relative to the residual solvent peak (δ = 2.50 ppm for ^{1}H and 39.52 ppm for ^{13}C) and coupling constants (J) are reported in Hz. Multiplicity was abbreviated as s (singlet), d (doublet), t (triplet), and m (multiplet). High-resolution mass spectra (HRMS) were recorded using a Q-TOF spectrometer equipped with electrospray ionization (ESI, 4000 V) in positive mode. The UV-Vis spectra were recorded using a Thermo Scientific Evolution 300 spectrophotometer over the range of 200–800 nm using quartz cuvettes of 1 cm path-length. Solvatochromic studies were conducted at a concentration of 20 μM in ethanol, acetonitrile, and dimethylsulfoxide. Differential scanning calorimetry (DSC) and thermogravimetric analysis (TGA) were performed using an STA7200 differential thermogravimetric analyzer under a nitrogen atmosphere. The band gap energies of compounds were determined using a Cary 100 spectrophotometer equipped with a diffuse reflectance accessory.

4.2 Microwave-assisted multicomponent synthesis of 4,6-diaryl-3-cyano-2(1*H*)-pyridones 4

A mixture of the corresponding aromatic aldehyde **1a–c** (3 mmol), acetophenone **2** (3 mmol, 350 μL), ethyl cyanoacetate **3** (3 mmol, 319 μL), and ammonium acetate (9 mmol, 694 mg) was prepared in ethanol (2 mL). The reaction mixture was irradiated in a sealed vessel using a microwave reactor (Anton Paar Monowave 400) at 100 °C for 30 min. After irradiation, the solvent was removed under reduced pressure using a rotary evaporator. The crude product was then purified by consecutive washes. The first wash involved a mixture of *n*-hexane and dichloromethane (5 : 1, v/v), which was repeated three times. This was followed by three washes with a mixture of *n*-hexane and ethanol (5 : 1, v/v). The resulting solid was transferred to a Büchner funnel and washed with a small amount of cold ethanol (1 mL) to remove any residual solvent. Finally, the product was dried under a vacuum to afford 3-cyano-2(1*H*)-pyridones **4a–c**. Crystals of compounds **4a–c** suitable for single-crystal X-ray diffraction analysis were grown by slow evaporation from a solution of compounds in a mixture of methanol and *N*,*N*-dimethylformamide (1 : 5, v/v) under ambient temperature and pressure conditions for two weeks.

4.2.1. 2-Oxo-6-phenyl-4-(4-tolyl)-1,2-dihydropyridine-3-carbonitrile 4a. Compound **4a** was obtained as a yellow solid (601 mg, 70% yield). Mp 315 °C (lit. 313–314 °C).[37] Crystallographic data for compound **4a** has been deposited in the Cambridge Structural Database (CSD) with the deposition number 2335843. FTIR-ATR: ν(N–H) 3100–2800, ν(C≡N) 2218, ν(C=O) 1639, ν(C=C) 1607, 1497, 1472, 1227, 1078, 918, 816, 768, 694, 637, 558, and 540 cm^{-1}. UV-Vis (20 μM in ethanol): 221 ($\lambda_{\max}$, $\varepsilon = 1.55 \times 10^{4}$ L mol^{-1} cm^{-1}, $\pi \rightarrow \pi^*$), 257 ($\varepsilon = 1.60 \times 10^{4}$ L mol^{-1} cm^{-1}, $\pi \rightarrow \pi^*$), 301 ($\varepsilon = 0.85 \times 10^{4}$ L mol^{-1} cm^{-1}, $\pi \rightarrow \pi^*$), and 365 ($\varepsilon = 1.20 \times 10^{4}$ L mol^{-1} cm^{-1}, $n \rightarrow \pi^*$(C=O)) nm. ^{1}H-NMR (400 MHz, DMSO-d_6): 2.39 (s, 3H, CH$_3$), 6.79 (s, 1H, H-5), 7.37 (d, J = 8.0 Hz, 2H, ArH), 7.49–7.57 (m, 3H, ArH), 7.64 (d, J = 8.0 Hz, 2H, ArH), 7.89 (dd, J = 7.8, 1.8 Hz, 2H, ArH), and 11.65 (br s, 1H, NH) ppm. ^{13}C-NMR (100 MHz, DMSO-d_6): 20.9 (CH$_3$), 97.8 (Cq, CN), 106.0 (CH, C-5), 116.8 (Cq, C-3), 127.7 (2CH, Ar), 128.2 (2CH, Ar), 128.9 (2CH, Ar), 129.3 (2CH, Ar), 131.1 (CH, Ar), 132.6 (Cq, Ar), 133.2 (Cq, Ar), 140.4 (Cq, Ar), 151.6 (Cq, C-6), 159.5 (Cq, C-4), and 162.5 (C═O, C-2) ppm. HRMS (ESI+): *m*/*z* calculated for $C_{19}H_{15}N_2O^+$ = 287.1179 [M + H]$^+$; found 287.1185.

4.2.2. 4-(4-Bromophenyl)-2-oxo-6-phenyl-1,2-dihydropyridine-3-carbonitrile 4b. Compound **4b** was obtained as a yellow solid (874 mg, 83% yield). Mp 344 °C (lit. 293–295 °C).[38] Crystallographic data for compound **4b** has been deposited in the Cambridge Structural Database (CSD) with the deposition number 2335844. FTIR-ATR: ν(N–H) 3100–2800, ν(C≡N) 2217, ν(C═O) 1636, ν(C═C) 1604, 1499, 1471, 1226, 1071, 1009, 910, 821, 767, ν(C–Br) 689, 609, and 547 cm^{-1}. UV-Vis (20 μM in ethanol): 217 (λ_{max}, $\varepsilon = 2.05 \times 10^4$, L mol^{-1} cm^{-1}, $\pi \to \pi^*$), 260 ($\varepsilon = 1.95 \times 10^4$ L mol^{-1} cm^{-1}, $\pi \to \pi^*$), 290 ($\varepsilon = 1.00 \times 10^4$ L mol^{-1} cm^{-1}, $\pi \to \pi^*$), and 368 ($\varepsilon = 1.35 \times 10^4$ L mol^{-1} cm^{-1}, n $\to \pi^*$(C═O)) ppm. ^{1}H-NMR (500 MHz, DMSO-d_6): 6.83 (s, 1H, H-5), 7.51–7.59 (m, 3H, ArH), 7.70 (d, *J* = 9.0 Hz, 2H, ArH), 7.79 (d, *J* = 8.5 Hz, 2H, ArH), 7.90 (d, *J* = 6.5 Hz, 2H, ArH), and 12.87 (br s, 1H, NH) ppm. ^{13}C-NMR (125 MHz, DMSO-d_6): 98.8 (Cq, CN), 105.6 (CH, C-5), 116.3 (Cq, C-3), 124.1 (Cq, Cp), 127.8 (2CH, C*o*′), 128.9 (2CH, C*m*′), 130.3 (Cq, C*i*′), 130.4 (2CH, C*m*), 131.2 (CH, C*p*′), 131.8 (2CH, C*o*), 135.2 (Cq, C*i*), 151.4 (Cq, C-6), 158.6 (Cq, C-4), and 161.7 (C═O, C-2) ppm. HRMS (ESI+): *m*/*z* calculated for $C_{18}H_{12}{}^{79}BrN_2O^+$ = 351.0128 [M + H]$^+$; found 351.0134.

4.2.3. 4-(4-Chlorophenyl)-2-oxo-6-phenyl-1,2-dihydropyridine-3-carbonitrile 4c. Compound **4c** was obtained as a yellow solid (828 mg, 90% yield). Mp 320 °C (lit. 288–289 °C).[21] Crystallographic data for compound **4c** has been deposited in the Cambridge Structural Database (CSD) with the deposition number 2335845. FTIR-ATR: ν(N–H) 3100–2800, ν(C≡N) 2217, ν(C═O) 1637, ν(C═C) 1603, 1490, 1338, 1226, 1179, 1092, 1013, 962, 908, 822, ν(C–Cl) 766 (ν C–Cl), 689, 624, and 547 cm^{-1}. UV-Vis (20 μM in ethanol): 222 (λ_{max}, $\varepsilon = 1.38 \times 10^4$ L mol^{-1} cm^{-1}, $\pi \to \pi^*$), 259 ($\varepsilon = 1.46 \times 10^4$, L mol^{-1} cm^{-1}, $\pi \to \pi^*$), 295 ($\varepsilon = 0.60 \times 10^4$ L mol^{-1} cm^{-1}, $\pi \to \pi^*$), and 368 ($\varepsilon = 1.21 \times 10^4$, n $\to \pi^*$(C═O)) nm. ^{1}H-NMR (400 MHz, DMSO-d_6): 6.84 (s, 1H, H-5), 7.51–7.59 (m, 3H, H*m*′, H*p*′), 7.64 (d, *J* = 8.4 Hz, 2H, H*m*), 7.77 (d, *J* = 8.8 Hz, 2H, H*o*), 7.90 (d, *J* = 7.2 Hz, 2H, H*o*′), and 12.88 (s, 1H, NH) ppm. ^{13}C-NMR (100 MHz, DMSO-d_6): 96.6 (Cq, CN), 106.1 (CH, C-5), 116.4 (Cq, C-3), 127.8 (2CH, C*o*′), 128.9 (2CH, C*m*), 129.0 (2CH, C*m*′), 130.3 (2CH, C*o*), 131.3 (CH, C*p*′), 132.3 (Cq, C*i*′), 134.8 (Cq, C*i*), 135.4 (Cq, C*p*), 151.3 (Cq, C-6), 158.5 (Cq, C-4), and 162.0 (C═O, C-2) ppm. HRMS (ESI+): *m*/*z* calculated for $C_{18}H_{12}{}^{35}ClN_2O^+$ = 307.0633 [M + H]$^+$; found 307.0636.

4.3 Single-crystal X-ray diffraction analysis

Single-crystal X-ray diffraction data for compounds **4a–c** were collected at 298 K using an Agilent SuperNova, dual, Cu at zero, Atlas four-circle diffractometer equipped with a CCD plate detector. CuKα radiation (λ = 1.54184 Å) was employed. The data collection, integration, and absorption correction were performed using the CrysAlis PRO software package.[39] Crystal structures of compounds **4a–c** were solved through an iterative algorithm,[40] followed by a difference Fourier map. Refinement of these structures was performed using SHELXL2018/3 software,[41] with all non-hydrogen atoms refined anisotropically. Hydrogen atoms were geometrically generated and placed at calculated positions using a rigid model (C–H = 0.93–0.96 Å, N–H = 0.86 Å), and constrained with U_{iso} values set to 1.2 times (for methyl groups) or 1.5 times (for other hydrogens) the equivalent U_{eq} value of the attached atom. During refinements, substitutional disorder was refined over Br and Cl atoms in compounds **4b** and **4c**. Molecular and supramolecular graphics were generated using the graphical software Mercury.[27]

4.4 Computational methods

All electronic structure calculations for compounds **4a–c** were performed using the Gaussian 09 software package.[42] Density functional theory (DFT) calculations were employed at the B3LYP/6-311++G(2df,2pd) level of theory. The molecular geometries of compounds **4a–c** were optimized in the gas phase and *in silico* solvent environments using the implicit polarizable continuum model (PCM) to represent ethanol, acetonitrile, and DMSO. All atomic coordinates were relaxed during the optimization process. The optimized geometries were confirmed as local minima on the potential energy surface (PES) by harmonic vibrational frequency calculations, ensuring the absence of imaginary frequencies. To aid in the assignment of UV-Vis spectral bands, vertical excitation energies and oscillator strength values (*f*) were calculated in the gas phase, and the simulated solvents using the time-dependent DFT (TD-DFT) method at the B3LYP/6-311++G(2df,2pd) level of theory. A total of five excited states were included in these calculations (N_{States} = 5). Natural bond orbital (NBO) population analyses were performed on the optimized gas-phase geometries to generate the frontier molecular orbital (FMO) surfaces. The GaussView graphical interface was used for the visualization of molecular structures,[43] the generation of simulated IR and UV-Vis spectra, and the depiction of molecular surfaces such as frontier orbitals.

Topological analysis of the electron density (ρ) within the crystalline packing of compounds **4a–c** was performed using the quantum theory of atoms in molecules and crystals (QTAIM-C) approach developed by Bader.[44] To represent the crystalline environment, a dimeric model was considered for each compound by extracting two symmetrically related molecules from the corresponding unit cell. The wavefunctions of these dimers were calculated using Gaussian 09 software at the B3LYP/6-311++G(2df,p) level of theory. These wavefunctions were then used as input for the AIM2000 program[45] to perform the QTAIM-C analysis. Critical points on the gradient vector field of the electron density ($\nabla\rho$) were located using Newton's method with a maximum of 120 iterations and a step size factor of 0.5. The nature of each CP was determined by analyzing its Laplacian ($\nabla^2\rho$) and eigenvalue properties. The molecular graphs were constructed following the established QTAIM-C protocol. This involved tracing the paths of steepest descent (downhill paths) from bond critical points (BCPs, (3,+1) CPs) and paths of steepest ascent (uphill paths) from ring critical points (RCPs, (3,−1) CPs). In addition, bond paths connecting neighboring BCPs were identified.

Intermolecular interactions in the crystal packing of compounds **4a–c** were investigated using Hirshfeld surface (HS) analysis.[29] CrystalExplorer21.5 software[30] was employed to generate the HS and associated two-dimensional fingerprint plots. The three-dimensional d_{norm} (normalized contact distance) HS map was generated for each compound. A standard surface resolution was used for HS generation, and a fixed color scale of −0.2023 to +1.3588 au was applied to represent the range of normalized contact distances.

Data availability

The data supporting this article have been included as part of the ESI.† The crystallographic data have been deposited with the Cambridge Crystallographic Data Center, CCDC, and are assigned the deposition codes 2335843 (**4a**), 2335844 (**4b**), and 2335845 (**4c**).

Author contributions

DH-R: investigation, methodology; DB: conceptualization, writing – original draft; HR: writing – review & editing; JAGC: computational analyses, methodology, writing – original draft; MAM: methodology, writing – original draft; J-CC: conceptualization, methodology, writing – original draft.

Conflicts of interest

There are no conflicts to declare.

Acknowledgements

The authors acknowledge Universidad Pedagógica y Tecnológica de Colombia and Universidad de los Andes. This work was funded by the Dirección de Investigaciones of Universidad Pedagógica y Tecnológica de Colombia through project SGI-3470 and the young researcher encouragement project SGI-3650. We express our gratitude to the National Cancer Institute (NCI) for conducting the anticancer screening of the compounds, to Universidad de Alcalá (Spain) for providing the NMR spectra, and to Dr Claudia Castañeda for acquiring the diffuse reflectance spectra.

References

1 A. Loppinet-Serani, F. Charbonnier, C. Rolando and I. Huc, *J. Chem. Soc., Perkin Trans. 2*, 1998, 937–942.
2 D. Hurtado-Rodríguez, A. Salinas-Torres, H. Rojas, D. Becerra and J.-C. Castillo, *RSC Adv.*, 2022, **12**, 35158–35176.
3 M. M. K. Amer, M. A. Aziz, W. S. Shehab, M. H. Abdellattif and S. M. Mouneir, *J. Saudi Chem. Soc.*, 2021, **25**, 101259.
4 S. Sangwan, N. Yadav, R. Kumar, S. Chauhan, V. Dhanda, P. Walia and A. Duhan, *Eur. J. Med. Chem.*, 2022, **232**, 114199.
5 Y. Zhang and A. Pike, *Bioorg. Med. Chem. Lett.*, 2021, **38**, 127849.
6 G. Yang, Y. Wang, J. Tian and J.-P. Liu, *PLoS One*, 2013, **8**, e74916.
7 M. D. Latham, C. K. King, P. Gorycki, T. L. Macdonald and W. E. Ross, *Cancer Chemother. Pharmacol.*, 1989, **24**, 167–171.
8 S. Bauer, M. C. Heinrich, S. George, J. R. Zalcberg, C. Serrano, H. Gelderblom, R. L. Jones, S. Attia, G. D'Amato, P. Chi, P. Reichardt, J. Meade, Y. Su, R. Ruiz-Soto, J.-Y. Blay, M. Mehren and P. Schöffski, *Clin. Cancer Res.*, 2021, **27**, 6333–6342.
9 S. J. Smith, G. T. Pauly, A. Akram, K. Melody, Z. Ambrose, J. P. Schneider and S. H. Hughes, *J. Acquired Immune Defic. Syndr.*, 2016, **72**, 485–491.
10 I. W. Flinn, S. O'Brien, B. Kahl, M. Patel, Y. Oki, F. F. Foss, P. Porcu, J. Jones, J. A. Burger, N. Jain, V. M. Kelly, K. Allen, M. Douglas, J. Sweeney, P. Kelly and S. Horwitz, *Blood*, 2018, **131**, 877–887.
11 M. G. Zauderer, P. W. Szlosarek, S. L. Moulec, S. Popat, P. Taylor, D. Planchard, A. Scherpereel, M. Koczywas, M. Forster, R. B. Cameron, T. Peikert, E. K. Argon, N. R. Michaud, A. Szanto, J. Yang, Y. Chen, V. Kansra, S. Agarwal and D. A. Fennell, *Lancet*, 2022, **23**, 758–767.
12 A. S. A. Alimmari, B. D. Božić, A. D. Marinković, D. Ž. Mijin and G. S. Ušćumlić, *J. Solution Chem.*, 2012, **41**, 1825–1835.
13 A. Marinković, D. Mijin, J. Mirković, V. Maslak and C. O. Kappe, *J. Serb. Chem. Soc.*, 2014, **79**, 759–765.
14 S. K. Rai, S. Khanam, R. S. Khanna and A. K. Tewari, *RSC Adv.*, 2014, **4**, 44141–44145.
15 K. Salamanca-Perdigón, D. Hurtado-Rodríguez, J. Portilla, I. Iriepa, H. Rojas, D. Becerra and J.-C. Castillo, *ChemPlusChem*, 2024, e202400172.
16 D. Becerra, R. Abonia and J.-C. Castillo, *Molecules*, 2022, **27**, 4723.
17 C. Simon, T. Constantieux and J. Rodriguez, *Eur. J. Org Chem.*, 2004, **24**, 4957–4980.
18 L. Rong, X. Li, H. Wang, D. Shi and S. Tu, *Chem. Lett.*, 2006, **35**, 1314c1315.
19 L. Rong, H. Wang, J. Shi, F. Yang, H. Yao, S. Tu and D. Shi, *J. Heterocycl. Chem.*, 2007, **44**, 1505–1508.
20 L. Rong, H. Han, H. Jiang, D. Shi and S. Tu, *Synth. Commun.*, 2008, **38**, 217–224.
21 H. A. El-Sayed, N. H. Ouf and A. H. Moustafa, *Res. Chem. Intermed.*, 2014, **40**, 407–412.
22 I. S. Antonijevic, G. V. Janjic, M. Milcic and S. D. Zaric, *Cryst. Growth Des.*, 2016, **16**, 632–639.
23 A. Nataraj, V. Balachandran and T. Karthick, *J. Mol. Struct.*, 2013, **1031**, 221–233.
24 P. Politzer and F. Abu-Awwad, *Theor. Chem. Acc.*, 1998, **99**, 83–87.
25 R. S. Mulliken, *J. Chem. Phys.*, 1934, **2**, 782.
26 R. G. Parr, L. von Szentpaly and S. Liu, *J. Am. Chem. Soc.*, 1999, **121**, 1922–1924.
27 C. F. Macrae, I. J. Bruno, J. A. Chisholm, P. R. Edgington, P. McCabe, E. Pidcock, L. Rodriguez-Monge, R. Taylor, J. van de Streek and P. A. Wood, *J. Appl. Crystallogr.*, 2008, **41**, 466–470.

28 P. L. A. Popelier, *Atoms in Molecules: An Introduction*, Pearson Education, Harlow, Great Britain, 2000.

29 M. A. Spackman and D. Jayatilaka, *CrystEngComm*, 2009, **11**, 19–32.

30 M. J. Turner, J. J. McKinnon, S. K. Wolff, D. J. Grimwood, P. R. Spackman, D. Jayatilaka and M. A. Spackman. *CrystalExplorer17*, University of Western Australia, 2017, available at: **https://hirshfeldsurface.net/**.

31 J.-C. Castillo, D. Becerra and M. A. Macías, *Crystals*, 2023, **13**, 694.

32 C. Serrano-Sterling, D. Becerra, J. Portilla, H. Rojas, M. Macías and J.-C. Castillo, *J. Mol. Struct.*, 2021, **1244**, 130944.

33 I. V. Magedov, M. Manpadi, M. A. Ogasawara, A. S. Dhawan, S. Rogelj, S. V. slambrouck, W. F. A. Steelant, N. M. Evdokimov, P. Y. Uglinskii, E. M. Elias, E. J. Knee, P. Tongwa, M. Y. Antipin and A. Kornienko, *J. Med. Chem.*, 2008, **51**, 2561–2570.

34 A. A. Fadda, K. S. Mohamed, H. M. Refat and E. E. El-Bialy, *Heterocycles*, 2015, **91**, 134–148.

35 M. I. Ansari, A. Arun, M. K. Hussain, R. Konwar and K. Hajela, *ChemistrySelect*, 2016, **1**, 4255–4264.

36 Y. Tangella, K. L. Manasa, V. L. Nayak, M. Sathish, B. Sridhar, A. Alarifi, N. Nagesh and A. Kamal, *Org. Biomol. Chem.*, 2017, **15**, 6837–6853.

37 R. Mekheimer, *Pharmazie*, 1994, **49**, 322–324.

38 L. Rong, H. Wang, J. Shi, F. Yang, H. Yao, S. Tu and D. Shi, *J. Heterocycl. Chem.*, 2009, **44**, 1505.

39 *CrysAlisPro 1.171.39.46e*, Rigaku Oxford Diffraction, 2018.

40 L. Palatinus and G. Chapuis, *J. Appl. Crystallogr.*, 2007, **40**, 786–790.

41 G. M. Sheldrick, *Acta Crystallogr., Sect. C: Struct. Chem.*, 2015, **71**, 3–8.

42 M. J. Frisch, G. W. Trucks, H. B. Schlegel, G. E. Scuseria, M. A. Robb, J. R. Cheeseman, G. Scalmani, V. Barone, G. A. Petersson, H. Nakatsuji, X. Li, M. Caricato, A. Marenich, J. Bloino, B. G. Janesko, R. Gomperts, B. Mennucci, H. P. Hratchian, J. V. Ortiz, A. F. Izmaylov, J. L. Sonnenberg, D. Williams-Young, F. Ding, F. Lipparini, F. Egidi, J. Goings, B. Peng, A. Petrone, T. Henderson, D. Ranasinghe, V. G. Zakrzewski, J. Gao, N. Rega, G. Zheng, W. Liang, M. Hada, M. Ehara, K. Toyota, R. Fukuda, J. Hasegawa, M. Ishida, T. Nakajima, Y. Honda, O. Kitao, H. Nakai, T. Vreven, K. Throssell, J. A. Montgomery Jr, J. E. Peralta, F. Ogliaro, M. Bearpark, J. J. Heyd, E. Brothers, K. N. Kudin, V. N. Staroverov, T. Keith, R. Kobayashi, J. Normand, K. Raghavachari, A. Rendell, J. C. Burant, S. S. Iyengar, J. Tomasi, M. Cossi, J. M. Millam, M. Klene, C. Adamo, R. Cammi, J. W. Ochterski, R. L. Martin, K. Morokuma, O. Farkas, J. B. Foresman and D. J. Fox, *Gaussian 09, Revision A.02*, Gaussian, Inc., Wallingford CT, 2016.

43 R. Dennington, T. Keith and J. Millam, *GaussView 6.0.16*, Semichem, Inc., Shawnee Mission, 2016.

44 R. F. Bader, *Atoms in Molecules: A Quantum Theory*, Oxford University Press, Oxford, 1990.

45 F. Biegler-Konig, J. Schonbohm and D. J. Bayles, AIM2000 – a program to analyze and visualize atoms in molecules, *J. Comput. Chem.*, 2001, **22**, 545–559.